

Radiation stability of mixed tin–lead halide perovskites: Implications for space applications

Brandon K. Durant^{a,*}, Hadi Afshari^a, Shashi Sourabh^a, Vishal Yeddu^b, Matthew T. Bamidele^b, Satyabrata Singh^c, Bibhudutta Rout^c, Giles E. Eperon^d, Do Young Kim^b, Ian R. Sellers^a

^a Homer L. Dodge Department of Physics and Astronomy, University of Oklahoma, 440 W. Brooks St, Norman, OK, 73019, USA

^b School of Materials Science and Engineering, Oklahoma State University, 526 N. Elgin Ave, Tulsa, OK, 74106, USA

^c Department of Physics, University of North Texas, 210 Ave A, Denton, TX, 76203, USA

^d Center for Chemistry and Nanoscience, National Renewable Energy Laboratory, 15013 Denver, West Parkway, Golden, CO, 80401, USA

ARTICLE INFO

Keywords:

Perovskite solar cells
Space photovoltaics
Proton irradiation
Radiation tolerance

ABSTRACT

Mixed organic-inorganic halide perovskite solar cells (PSCs) have received considerable attention in recent years for their impressive solar to electrical power efficiency gains and potentially lower material and processing costs for optoelectronic applications. In addition to terrestrial applications, PSCs are of interest to the space power markets for their low cost, low weight, adaptability to flexible architectures, and tolerance to high energy particle irradiation (mainly protons and electrons). Here we investigate the properties of mixed formamidinium-methylammonium tin-lead iodide (FASn)_{0.6}(MAPb)_{0.4}I₃ perovskites which lower the lead content as well as the bandgap, making them attractive for the low bandgap absorber material in tandem PSCs. Through current density-voltage (*JV*) characterization at lower temperatures, majority carrier transport is hindered and a barrier to photogenerated carrier extraction is evident. This is attributed to the thermally induced change of the bandgap of the absorber layer relative to the energy selective contacts in the device. We find that although the architecture used here hinders the performance at temperatures below 225 K, the tolerance to high energy (3.7 MeV) protons is impressive, considerably out-performing commercially available thin-film CIGS. These results suggest further improvements to structural and interface stability as well as lightweight encapsulation could lead to all perovskite flexible tandem arrays deployed for power generation on missions to low Earth orbit, the moon, Mars, and beyond.

1. Introduction

Perovskite solar cells (PSC) are a leading material being investigated to disrupt the current photovoltaics (PV) industry. Although issues of stability are persistent, record efficiencies of >25% [1] are impressive for such an immature material and have garnered the interest of research groups worldwide. With a composition of earth abundant elements, solution-based deposition techniques, moderate annealing temperatures, and high absorption coefficient and therefore require thin active layers, PSCs are attractive candidates for lowering the cost of photovoltaic devices. Additionally, the composition of cations and halides that comprise the perovskite tunes the bandgap of the material [2]. Research has grown from single junction perovskite solar cells with an ideal bandgap energy near 1.5 eV and maximum theoretical efficiency of 30% [3], to wide bandgap energy adaptable to the top cell for tandem

photovoltaic devices with a maximum theoretical efficiency of 46% [4] by reducing the thermalization and transmission losses [5]. This tunability has led to impressive tandem efficiencies in Perovskite/Si [6, 7], Perovskite/CIGS [8–10], and all perovskite devices [6,11–15] among other structures. Like many other polycrystalline thin film PV materials, PSCs are adaptable to flexible architecture. Many of the high-quality devices utilize organic based carrier selective contacts or otherwise flexible motifs including fabrication on flexible substrates. Such architectures could serve to increase production throughput in a so-called “roll-to-roll” fashion which could further lower costs and speed up deployment.

In space environments, PV systems are the leading method of power supply for not only near-Earth missions, but also missions extending to the moon, Mars, and deep space. This is primarily due to the absence of fuel, and therefore a high specific power (power/mass) comparable

* Corresponding author.

E-mail address: bdurant@ou.edu (B.K. Durant).

<https://doi.org/10.1016/j.solmat.2021.111232>

Received 26 February 2021; Received in revised form 5 May 2021; Accepted 9 June 2021

Available online 22 June 2021

0927-0248/© 2021 Elsevier B.V. All rights reserved.

mainly to nuclear fission based remote power generation. The other two main criteria considered for space power solar cells are the satellite form factor and so-called end of life (EOL) performance. The satellite form factor is determined by the rigidity or, conversely, the flexibility of the solar arrays. Flexible all perovskite tandem solar arrays would be attractive for a completely flexible array that could be stored in a small volume providing protection during launch and prior to deployment. In addition, dynamic control of such arrays would prevent damage when the satellite encounters the harsh radiation environments during the mission. End of life performance is primarily determined by the susceptibility of the solar arrays to degradation of power generation from radiation exposure in the harsh environments of space. Extending the EOL performance enables new mission profiles such as higher latitude coverage of the new Starlink, Telesat, and upcoming OneWeb communication satellite constellations providing uninterrupted internet services worldwide with greater navigation accuracy [16]. Such missions could involve polar low Earth orbits (LEO) or possibly highly eccentric orbits (HEO) and therefore much greater fluences of the trapped particles in the Van-Allen belts [17]. To overcome large fluences, the III-V based multijunction devices used currently must incorporate thicker, heavier, and therefore costly protective encapsulation [18].

Recently, several groups have shown the impressive tolerance of PSCs to proton irradiation in single junction perovskite based solar cells and tandem devices [19–26]. In order for perovskite only tandem solar devices and arrays to become reality, a lower bandgap perovskite than the more well studied lead iodide absorbers must be incorporated into the stack. Much research has focused on mixing organic/inorganic cations into the A site as well as mixing halide constituents to adjust the bandgap lower. One of the attractive candidates is the family of tin based perovskites that have a generally lower band gap, calculated to be from 0.75 eV to 1.3 eV for CsSnX_3 mixed halides [27]. The highest reported lead free tin based perovskite efficiency of over 13% still lags behind the lead based counterparts and suffer from stability issues [28]. The stability issue with the pure tin-based perovskites can however be mostly mitigated by alloying with Pb, to form mixed tin-lead perovskites. These materials have bandgaps as low as 1.2eV, and have shown Voc deficits approaching the theoretical limits [29]. Additionally, comparing crystallographic data of MAPbI_3 and FASnI_3 , the density of the material decreases from 4.092 g/cm³ to 3.649 g/cm³ which could serve to lower the interaction of high energy particles on the lattice and possibly the induced vacancies and defects [30].

Recently, CIGS/perovskite tandems have been considered for their potential for space power applications. These reports [22,24] indicate that perovskites represent a significant improvement in terms of radiation tolerance to thin films CIGS. Recently, the stability and performance of flexible CIGS has been accessed for space applications specifically with respect to the low-intensity low-temperature, or LLT, conditions consistent with Jupiter and Saturn [31,32]. While these CIGS demonstrated considerable tolerance to the low irradiance and hostile thermal conditions of deep space and space travel, in general, their tolerance to radiation is less than currently attributed to the perovskite systems [22, 24]. To further assess these conclusions, here, the stability of single band gap $(\text{FASn})_{0.6}(\text{MAPb})_{0.4}\text{I}_3$ solar cells are assessed under comparable conditions to that of thin film CIGS solar cell previously assessed in our laboratory to provide further insight into the relative performance of these thin film technologies and to recent works on tandem solar cells in these systems.

2. Materials and methods

Mixed formamidium-methylammonium tin-lead iodide $(\text{FASn})_{0.6}(\text{MAPb})_{0.4}\text{I}_3$ solar cells were fabricated by adopting methods described previously [33].

2.1. Materials

All the materials were used as is without any purification. Lead iodide (PbI_2 , 99.999%), lead thiocyanate ($\text{Pb}(\text{SCN})_2$, 99.9%) and tin fluoride (SnF_2 , 99.99%) were purchased from Millipore-Sigma. Formamidinium iodide (FAI) and methylammonium iodide (MAI) were purchased from GreatCell Solar Materials. Tin iodide beads (99.999%) were purchased from Alfa Aesar [6,6].-Phenyl-C61-butyric acid methyl ester (PC_{61}BM) was purchased from Nano-C. 1,3,5-Tri(*m*-pyridin-3-ylphenyl)benzene, 1,3,5-Tris(3-pyridyl-3-phenyl)benzene (TmPyPB) and C60 were purchased from Lumtec. The supplier of poly(3,4-ethylene dioxothiophene) polystyrene sulfonate (PEDOT:PSS) (Clevios P VP Al 4083) was Heraeus Precious Metals.

2.2. Perovskite precursor solution preparation

For the precursor solution preparation, 691.5 mg of PbI_2 , 238.5 mg of MAI and 16.95 mg of $\text{Pb}(\text{SCN})_2$ were dissolved in 1.5 ml of DMF: DMSO mixture (9:1 vol ratio) to make a MAPbI_3 solution. The FASnI_3 solution was prepared by dissolving 258 mg of FAI, 558 mg of SnI_2 and 23.4 mg of SnF_2 in 1.5 ml of DMF: DMSO mixture (4:1 vol ratio). These solutions were stirred for 1 h. Prior to spin coating stoichiometric amounts of the FASnI_3 and MAPbI_3 solutions were mixed and stirred for 1 h to produce the $(\text{FASn})_{0.6}(\text{MAPb})_{0.4}\text{I}_3$ perovskite precursor solution. The processing of perovskite precursor solution was done entirely inside a nitrogen filled glovebox.

2.3. Solar cell fabrication

Prepatterned indium tin oxide (ITO) coated glass substrates were cleaned by ultrasonication for 30 min each in water, acetone and isopropyl alcohol. A 30-min UV-ozone treatment was performed prior to spin coating. PEDOT:PSS was spin coated on the substrates at 4000 rpm for 1 min and annealed at 175 °C for 10 min in ambient conditions. The substrates were then transferred to a nitrogen filled glovebox for the deposition of perovskite precursor solution. Prior to spin coating, the perovskite precursor was filtered using 0.45 μm polytetrafluoroethylene (PTFE) filter and spin coated at 5000 rpm for 1 min. After 12 s of spin-coating, 1 ml of chloroform was dropped onto the substrates. The perovskite coated films were annealed at 100 °C for 5 min. PC_{61}BM (20 mg/ml in chlorobenzene) was then spin coated at 4000 rpm for 1 min 20 nm of C60, 8 nm of TmPyPB, and 100 nm of silver were then deposited by thermal evaporation. Devices were kept in a nitrogen box atmosphere and no antireflective coatings were employed. The device encapsulation was done using a 100 μm thick microscope coverslip and UV curable epoxy for 10 min. Device contact areas were 0.09 cm² while a circular aperture (0.01886 cm² area) was used for illumination.

2.4. Device characterization

Temperature dependent current density-voltage (*JV*) curves were collected using a silicon solar cell calibrated solar simulator (Newport) with AM0 filter, Keithley 2400 voltage and current source at a sweep rate of 333 mV/s, and a dwell time of 30 ms. Devices were mounted in a Linkam liquid nitrogen cooled stage within an in-house built cryostat stage for 2-electrode connections. Temperature dependent external quantum efficiency (EQE) measurements were performed with monochromatic quartz tungsten halogen lamp illumination, preamplifier and lock-in amplifier (Stanford) at short circuit (*Jsc*) conditions. Room temperature measurements were performed under dry nitrogen atmosphere, while temperature dependent measurements were performed under vacuum. No light soaking or bias preconditioning of the cells were performed.

Prior to the experiment, the interaction of energetic protons into the target layers was simulated using a well-known ion-solid interaction codes: The Stopping and Range of Ions in Matter (SRIM-2013) [34]. The

SRIM code is a Monte Carlo simulation based on the binary collision approximation (BCA), where the ions travel through the target material by experiencing many independent collisions with the atoms in the target. The energy loss occurs via two separate mechanisms called electronic ionization loss and nuclear displacement loss. The electronic energy loss refers to the loss of energy of the incident ion to the electrons of the target atoms. This is sometimes referred to as inelastic energy loss. This energy is responsible for the ionization of electrons in the target atoms resulting in local heating. Nuclear energy loss refers to the loss of energy of the incoming ion to the target nuclei; so-called elastic energy loss. The nuclear collision can cause target atoms to be displaced from their regular lattice site creating vacancies. In order to estimate the total damages (vacancies and displaced atoms), “Full cascade” calculations were performed for 200,000 ions with 3.7 MeV proton ions and scaled up to the desired fluence. The proton energy was chosen in such a way that the majority of the proton ions travel through the back encapsulation glass as well as the absorber layer and deposit in the front-side glass superstrate (relative to incident light). The details of the target layer composition is provided in the supplementary information while the range of the proton beam is illustrated in Fig. 3.

The proton irradiation experiment was performed using a high-energy ion irradiation beamline associated with a tandem ion accelerator (9SDH-2, NEC) facility at the Ion Beam Modification and Analysis Laboratory (IBMAL) of the University of North Texas (UNT) [35]. Each sample received a fluence of 1×10^{11} protons/cm² with a beam flux of 3×10^9 particles/cm²/second through the back encapsulation glass slide (100 μ m), and silver back contact (see Figure S17 for illustration). This was opposite to the side in which illumination was performed on the thick 1 mm glass substrate which was too thick to be penetrated by low MeV proton energies.

These conditions qualitatively reproduce those used to irradiate unencapsulated CIGS in earlier works [31,32] and therefore allow the assessment of the relative performance and degradation of the (FASn)_{0.6}(MAPb)_{0.4}I₃ solar cells under investigation here with the commercial single junctions CIGS solar cells assessed previously.

3. Results and discussion

Fig. 1(b) shows the current density – voltage (*J-V*) for a studied (FASn)_{0.6}(MAPb)_{0.4}I₃ device with relatively high performance in the dark (black) and under 1-sun AM0 illumination at 300 K. Under these conditions the device has a *V*_{oc} of 0.77 V and *J*_{sc} of 31.4 mA/cm². Considering the fill factor of 71%, the power conversion efficiency of this device was 12.8%. Statistics of 15 devices are presented in Table SI 2. Fig. 1(c) shows a comparison of the EQE and PL at 300 K. When considering the extracted *J*_{sc} at 25.8 mA/cm² (AM0) from the EQE

spectrum (Fig. SI 4(a)), the 1 sun *J*_{sc} is over estimated due to the mismatch of solar simulator spectrum, which is the calibrated to the visible regime. Both emission and the onset of absorption are well matched and indicate bandgap of 1.24 eV, which is consistent with the Sn composition in the perovskite absorber used here (60%). On inspection, the EQE shows a loss of carrier extraction at > 800 nm (see Fig. 1(c)), which indicates limited absorption of these thin 550 nm absorber layers [11]. However, this does not affect the conclusion of the work presented here. In order to deconvolute the impact of the tests we carried out on the perovskite absorber versus the organic contact materials, we also fabricated organic-only control devices – the same structure but without any perovskite. Shown in Fig. 1(b) and (c) are the light *JV* and EQE, respectively of an organic only reference solar cell (ITO/PEDOT/PCBM/C60/TmPyPB/Ag) fabricated alongside the perovskite structure under investigation. The limited contribution of the organic part of the solar cell is confined entirely to the UV region, and therefore has negligible contribution to the loss of EQE from the perovskite devices at >750 nm.

It is well known Sn–Pb based perovskites have limited minority carrier diffusion lengths with respect to state-of-the-art Pb-based systems, due to the prevalence of Sn⁴⁺ and the local strain and vacancies this small ion induces in the lattice. The net result is an increase in the p-type background doping and non-radiative centers in the absorber, both of which limit minority electron transport in the mixed Pb–Sn perovskite [36,37]. The effect of the p-type nature of the perovskite is a shift in the position of the Fermi-level closer to the valence band. Here, the shifting of the Fermi-level could eventually lead to a decreased space charge width at the hole selective PEDOT:PSS contact layer and eventually a small barrier or non-ideal interface to holes. This would result in recombination losses, particularly at lower temperatures – due to the narrower perovskite bandgap – and upon radiation exposure, both of which are discussed below. Here, the net result from these properties is limited carrier transport, with the loss of hole extraction from deeper in the perovskite absorber layer, and recombination with minority electrons in the p-type absorber in the samples measured in this work. A similar argument could be postulated for the electron selective contact but it is known in these systems that the hole selective contact appears to be the site of diminished carrier extraction and interfacial decomposition [36,38].

The effect of temperature on the performance of the (FASn)_{0.6}(MAPb)_{0.4}I₃ solar cell is illustrated in Figure(s) 2(a) and (b), which show the temperature dependent *JV* under 1-sun AM0, and the temperature dependent EQE, respectively. Temperature dependence of all *JV* parameters are shown in Fig. SI 2. In Fig. 2(a) the *J*_{sc} decreases from ~35 mA/cm² at 77 K to ~30 mA/cm² at 300 K, which is consistent with the dependence of the total EQE (Fig. 2(b)), which also scales with

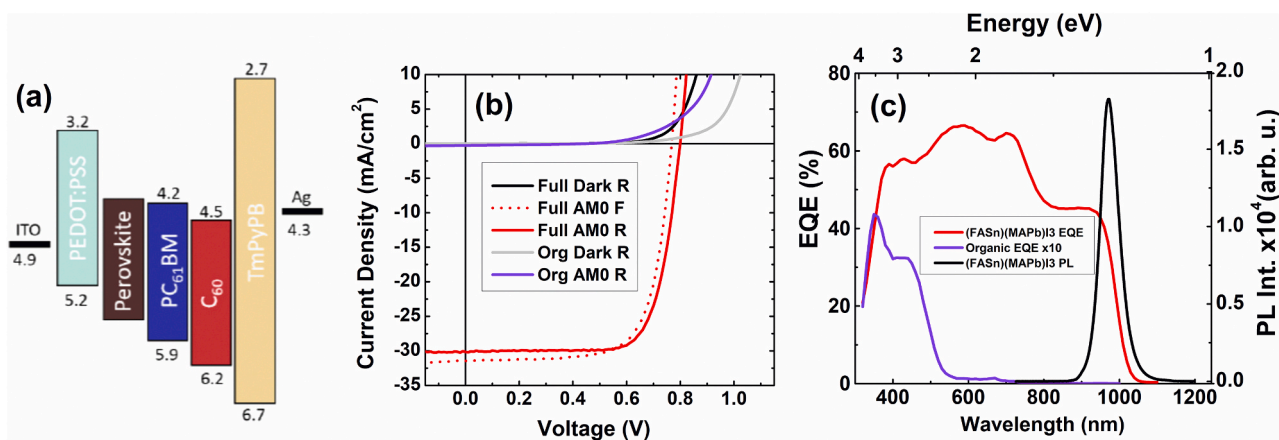


Fig. 1. (a) Shows a schematic of the band alignment of the device under investigation. The left side being the light illumination side. (b) Dark *JV* and light *JV* under 1-sun AM0 at 300 K. with a PCE ~13%. (c) Comparison of the EQE and PL at 300 K showing a band gap of ~1.24 eV for the (FASn)_{0.6}(MAPb)_{0.4}I₃ absorber.

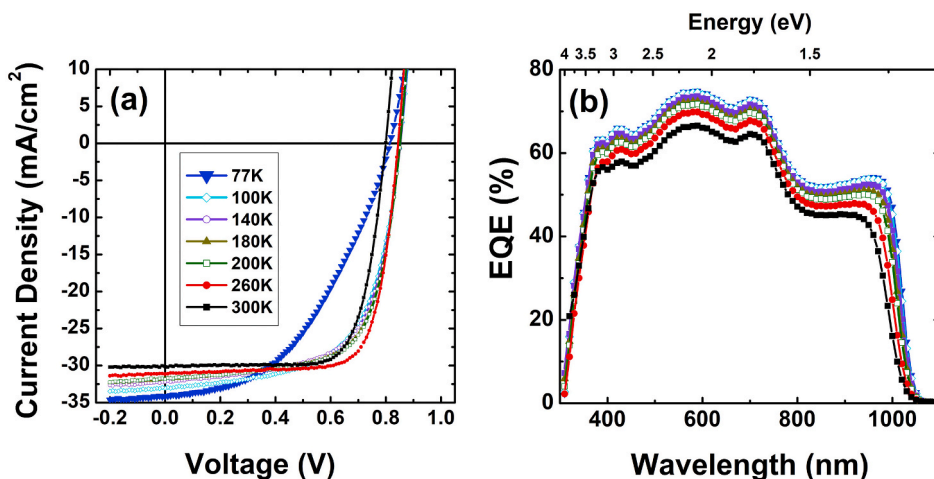


Fig. 2. Temperature dependent (a) J - V and (b) EQE from 77 K to 300 K. The $(\text{FASn})_{0.6}(\text{MAPb})_{0.4}\text{I}_{0.3}$ experiences a structural phase evolution at 100 K.

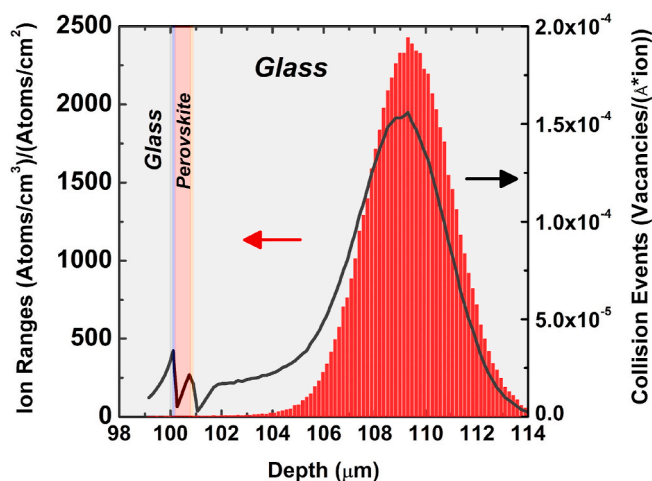


Fig. 3. Stopping and Range of Ions in Matter (SRIM) calculations for ion ranges (left axis, red bars) and collision events (right axis, black line) of 3.7 MeV protons into back surface of perovskite solar cell. The target was encapsulated with 100 μm cover glass. The range of the ions was approximately 10 μm into the front glass superstrate. Material details are provided in the supplemental information. (For interpretation of the references to colour in this figure legend, the reader is referred to the Web version of this article.)

temperature. This change can be well understood in terms of the decrease in the perovskite bandgap at lower temperatures [39–41], which is supported, not only the increasing current, but the reduced voltage, in addition to the temperature dependent shift in absorber edge observed in the EQE shown in Fig. 2(b).

Along with the typical temperature dependent characteristics of the perovskite, a strong reduction in the fill factor is also evident below 100 K (<60%), which softens between 100 K and 200 K (~65%), before an increase in the FF (>75%) and more conventional operation is observed above 260 K (Fig. SI 2(a)). Such inflections in the PV response under illumination have been attributed to parasitic barriers and are seen across several systems in which, barriers or non-ideal interfaces are present [42]. There is also a known phase transition for the formamidinium tin-lead iodide perovskites near 100 K believed to be between two distinctly different orthorhombic phases, which also abruptly changes the bandgap of the perovskite [40]. Temperature dependent crystallographic studies of this particular composition however have not been performed yet. Here, therefore it is suspected that the large barrier and associated loss in fill factor in the JV below 100 K is due the

unfavorable band offsets (See Fig. 1(a)) between the $(\text{FASn})_{0.6}(\text{MAPb})_{0.4}\text{I}_{0.3}$ and the other constituent layers in the device structure, which inhibit carrier extraction at lower temperature. Between 100 K and 200 K this effect is reduced but not removed. This particular perovskite shows an orthorhombic structure at room temperature. While the tin based FASnI_3 is known to undergo a phase transition from cubic to tetragonal between 250 and 275 K [43], and lead based MAPbI_3 transitions from tetragonal to orthorhombic around 125 K. The mixed $(\text{FASn})_{0.6}(\text{MAPb})_{0.4}\text{I}_{0.3}$ perovskite under investigation here appears to remain structurally stable down to around 100 K [40]. Although extensive temperature dependent materials characterization is still needed for this particular composition, poor FF and inhibited extraction between 225 K and 100 K are not therefore thought to be due to a phase transition, but rather the continued presence of a (albeit smaller) barrier, and the temperature dependence of the perovskite bandgap relative to one of the carrier selective contacts. Above 225 K, the carrier extraction and therefore device performance are maximized with a PCE of 14.5% at 260 K. This is the result of a combination of an improved FF (75%) and optimum V_{oc} (0.84 V) at 260 K, which falls off with bandgap renormalization at 300 K.

The effects on the temperature dependent J - V are well reflected in the EQE measurements shown in Fig. 2(b). The maximum EQE is evident below 200 K, and decreases monotonically with temperature until ~260 K. The temperature dependence of the bandgap is also evident with increasing temperature, with the well-known increase in perovskite energy gap observed as the lattice temperature increases [39–41]. The systematic decrease of the total EQE with increasing temperature – rather than a modulation of the shape in certain spectral regions – supports the presence of a parasitic barrier rather than recombination losses or inhibited carrier mobility in specific regions of the device. It has been shown the mixed tin-lead systems have a lower Fermi-level relative to the pure lead systems and even allow a Schottky junction to form between the active perovskite and ITO contact without a dedicated PEDOT:PSS hole selective contact [38]. Lower temperatures can lead this Fermi-level to shift to higher energies as the conduction band and (even more so) the valence band shift to higher energies with decreasing temperature [44]. Lower temperatures may serve to lower the self p-doping of the tin based perovskites and extending the depletion region deeper into the absorber region, increasing the carrier collection at short circuit conditions. A barrier to minority holes in the valence band, however, appears to begin to form at positive voltages, leading to a decreased fill factor. Additionally the conductivity of PEDOT:PSS has been shown to decrease at low temperatures due to the crystallization of water which would also serve to lower the fill factor [45,46]. Although the loss in FF inhibits the PCE (as seen in Fig. SI 2) at temperatures below

275 K, the relatively stable performance down to 100 K shows promise if alternate structures and junctions are developed for this particular system. It is also evident that the peak performance at 260 K still makes this material a good candidate for near Earth, lunar and Martian missions.

While improvements in device performance and stability certainly require optimization, the mixed Sn–Pb perovskites are attracting significant attention - not only for their more optimum bandgap with respect to the solar spectrum [3,47] - but as the bottom junction for all perovskite tandems, the efficiencies of which have now reached greater than 25% [13,48–53]. While these results are encouraging, it is important to understand the stability of single junction (FASn)_{0.6}(MAPb)_{0.4}I₃ solar cells as standalone systems to direct radiation, outside of its inclusion in tandem structures. While evidence that thermal cycling is of importance to these systems, here we focus solely on the effects of their proton radiation tolerance.

To perform such an assessment, proton irradiation was carried out on the same cells as presented in Figure(s) 1 and 2 (image in Fig. SI 6). These devices were encapsulated with a 100 μm cover slip glass and exposed to fluences of 1×10^{11} protons/cm². Stopping range of ions in Matter (SRIM) simulations were performed to determine the position of the protons with respect to the layers of the solar cell. At 3.7 MeV energies, this would be an integrated proton fluence equivalent to 4 years in a polar orbit such as heliosynchronous or approximately 17.4 h for the very high radiation flux environment of Jupiter's moon Europa according to SPENVIS calculations in Figure SI5 [54].

As seen in Fig. 3, the range of the protons of 3.7 MeV is primarily past the absorber layer and into the glass superstrate. Due to the low density (relative to the silver) the interactions of the high energy protons even after 100 μm cover slip glass is low and mostly electronic (ionizing) rather than nuclear hard-sphere collisions. This is partially due to the low density of the perovskite layer but also the energy of the protons passing through a thin 550 nm layer of material.

Fig. 4(a) shows the SRIM simulation results for the distribution of the total vacancy created due to the collision events between incident protons (energy of 3.7 MeV and fluence of 10^{11} H⁺/cm²) and host atoms in the various layers that constitute the solar cell architecture. The defect density gradually increases as protons penetrate deeper into the perovskite absorber layer. In the SRIM calculation, for the metal target atoms (Ag, Na, Ca, In, Sn, Pb) as well as for iodine a displacement energy of 25 eV was considered to estimate the damages. The displacement energy is the minimum energy needed to displace an atom to create a vacancy. For the lighter elements like H the displacement energy was 10 eV, whereas a displacement energy of 28 eV was used for O, C, and N. Fig. 4(b) shows the individual contributions of the vacancies associated with the constituent elements in the perovskite layer. The vacancies due to iodine are the major contributions (~50%) to the total vacancies, while Sn and Pb contribute less than 10% of the total vacancies. The H atoms present in the layer contribute to slightly above 10% of the total vacancies. The total number of vacancies produced per depth in the perovskite layer is comparable to the total vacancies produced per depth in our previously reported CIGS layer subject to 1.5 MeV proton irradiation for a similar fluence. Conservation of mass and charge would dictate that the vacancies produced would also result in other defects such as interstitials and antisites which would be paramount in determining the exact nature and consequences of each type of defect. However, in this work, we believe these calculations best represent the consequences of proton irradiation in the absorber lattice.

Figure(s) 5 shows the effects of irradiating a device with 3.7 MeV protons at 1×10^{11} protons/cm². Fig. 5(a) and (c) show the dark and 1-sun AM0 before (black) and after (red) exposure, respectively. Interestingly, despite considerable exposure to high energy protons, no significant leakage in dark *J-V* Fig. 5(a)) is evident, which is reflected in retention of the V_{oc} in Fig. 5(c). Indeed, these data suggest that the dark current above turn on is actually slightly less in the irradiated cell, which we return to below. The loss that is clearly observable in the performance of the irradiated solar cell is reflected to an increase in series

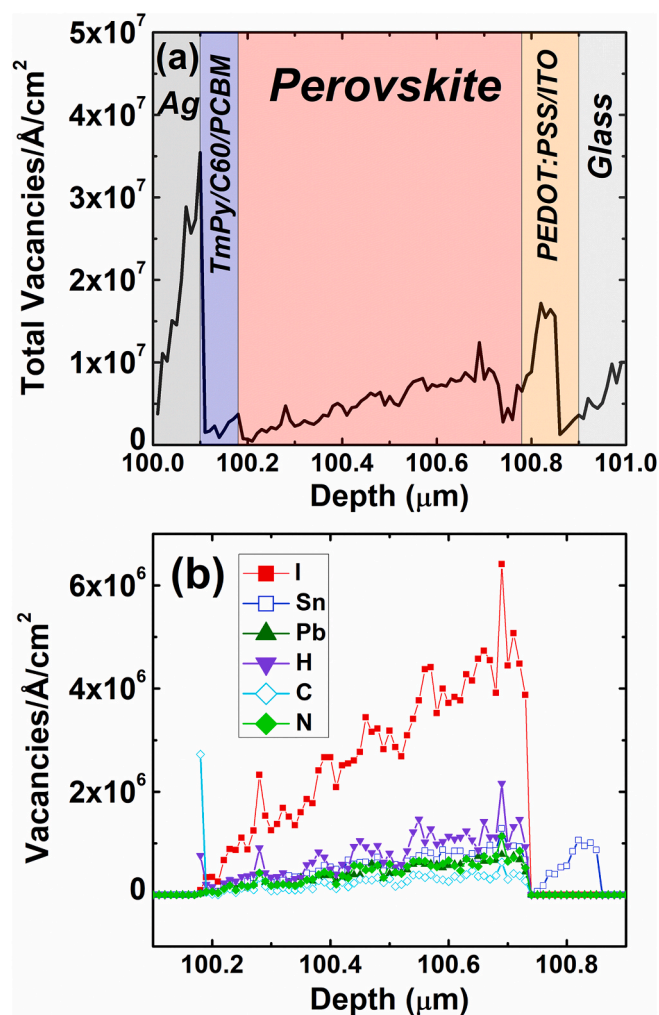


Fig. 4. (a) SRIM simulated damages in the target layer due to the irradiation of 3.7 MeV Protons with a fluence of 1×10^{11} ions/cm². The target was encapsulated with 100 μm cover glass. (b) Individual contributions of vacancies associated with the individual elements I (red, filled squares), H (violet, upside down triangles), Sn (blue, open squares), C (cyan, open circles), N (green, diamonds), and Pb (olive, triangles) in the perovskite layer are also shown. (For interpretation of the references to colour in this figure legend, the reader is referred to the Web version of this article.)

resistance above turn on and a subsequent reduction in the FF (from 70.0 to 69.6%), leading to a reduction in the J_{sc} (Fig. 5(c)) from 31.2 to 28.8 mA/cm², before and after irradiation, respectively. Although there was a mismatch between extracted J_{sc} from the EQE spectra and J_{sc} measured at 1-sun AM0, the effects of proton irradiation are relative and comparable for the same device. CIGS by comparison has a significant loss of V_{oc} of over 200 mV at the same light intensity and temperature, which was attributed to the increase in defects at grain boundaries and associated increase in dark current density [31]. See Supplementary Information Fig. SI 2 and Table SI 1 for the direct comparison of device performance.

The loss of J_{sc} is directly reflected in the EQE comparison shown in Fig. 5(b). Upon exposure to protons the EQE is slightly reduced uniformly across the spectrum. Similar behavior was observed in the temperature dependent EQE described above, which was attributed to the presence of a temperature dependent barrier to carrier collection as the (FASn)_{0.6}(MAPb)_{0.4}I₃ bandgap decreased at lower temperatures; resulting in unfavorable band alignment to minority carrier transport through the solar cell. The combination of the global loss of EQE – or reduced J_{sc} – despite the retention of the dark current/ V_{oc} , coupled with

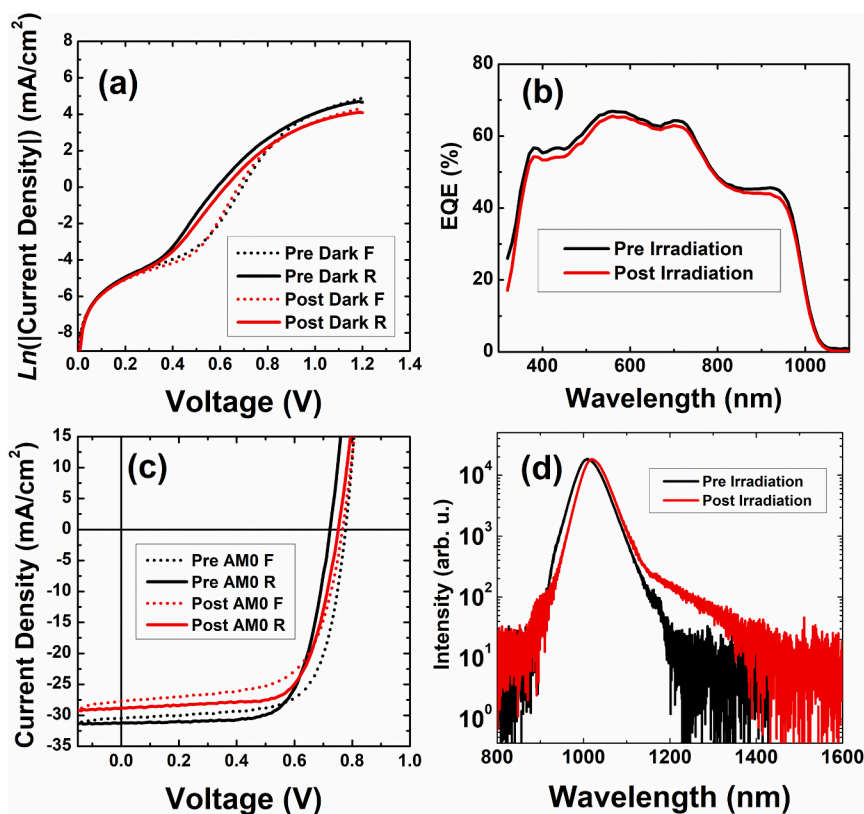


Fig. 5. (a) Comparison of the dark J - V , (b) EQE, (c) J - V under 1-sun AM0, and (d) photoluminescence at 300 K before (black) and after (red) proton irradiation of 1×10^{11} protons/cm². (For interpretation of the references to colour in this figure legend, the reader is referred to the Web version of this article.)

the increased resistance in the J - V measurements indicate that the predominant loss process after radiation is not significant non-radiative recombination, or leakage, but the radiation dependent creation of a parasitic barrier to photogenerated minority carriers. The dark current turn on is also slightly shifted to higher potentials alluding to a shifting potential necessary to transport majority carriers across the device. Indeed, the relative stability of the absorber to proton irradiation of the perovskite supports previous findings of the tolerance of the systems [19–22,24].

The bulk absorber stability is independently observed in this single junction system and moreover shows that in terms of radiation tolerance, these systems, in general, out-perform commercial CIGS under high levels of proton irradiation. Indeed, under similar levels of proton irradiation and vacancy creation, CIGS lose 14.3% of V_{oc} , 22.6% J_{sc} , and 16.4% FF, resulting in an overall relative loss in PCE of 44.6% (see supplementary information Figure SI2 and Table SI I). This as compared to 4.0% gain in V_{oc} , 7.7% loss in J_{sc} , 0.6% loss in FF totaling a mere 4.6% relative loss in PCE for the (FASn)_{0.6}(MAPb)_{0.4}I₃ perovskite assessed here. The relative degradation of performance between the sample under investigation here, and the CIGS in Refs. [2,31] appears related the difference in parasitic losses induced by irradiation in these two systems. The CIGS was however irradiated through the thin front contact as opposed to the back for the perovskite device, and the absorber thickness of the CIGS is $\sim 3x$ as thick which increases the interaction length for proton damage and (inherently) the number of defects produced. But, we believe the irradiation tolerance for perovskites still appears superior since the vacancy generation per depth is similar for both materials (Figure SI1) while the device performance is quite different. Here, in (FASn)_{0.6}(MAPb)_{0.4}I₃ the primary defect appears related to iodide displacement, which induces shallow defects, the mobile nature of which facilitates self-healing [19,25,55,56]. Furthermore, Sn⁴⁺ vacancies, which form close to grain boundaries and at interfaces [38], result in fewer non-radiative losses in the bulk absorber [24].

Indeed, the thermal degradation in low gap mixed Sn–Pb perovskites has also been shown to lead to oxidation and Sn-vacancies at the perovskite-PEDOT:PSS interface [24,36,38], which would lead to a barrier to minority carrier extraction. In the case of CIGS, several shallow vacancies in addition to deep Cu-vacancies are formed [22,31,57], which can be particularly parasitic and induce significant non-radiative losses. Indeed, while perovskites have now shown stable performance under proton irradiation of 1×10^{14} protons/cm² [24], levels in excess of 1×10^{13} protons/cm² produce complete loss of performance to thin film CIGS [31].

The losses induced in the narrow gap perovskite assessed here appear consistent with those of other perovskite systems assessed under high irradiation levels in that defect formation – or irradiation – appears to result in inhibited carrier collection through the formation of parasitic barriers or unbalanced minority carrier collection, rather than SRH losses in the absorber [19–22,24]. Evidence of decreased carrier collection is apparent in the loss of J_{sc} in Fig. 5(c). An increase in resistance for photogenerated carriers is also noticeable with a loss in fill factor and lower forward bias current density (shallower slope after turn-on). The V_{oc} however remains relatively unchanged. Brus et al., reported similar findings in MAPbI₃ based solar cells where it appeared the shunt and series resistances increased and diode ideality factor decreased leading to the conclusion that the leakage current due to SRH recombination and physical shunts at grain boundaries was actually reduced after irradiation [20]. Although the V_{oc} and FF did not increase considerably with these particular devices, the post-irradiated perovskite devices could be considered as partially compensated relative to the pre-irradiated devices, which are more intrinsic with more deep level recombination centers due to iodide vacancies but more p-type doping due to tin vacancies [58]. These effects are different than most other inorganic technologies exposed to proton irradiation where the dark currents usually increase due to shunting and increased SRH recombination due to deep level defect formation within the band gap

and the subsequent decrease in V_{oc} .

The high optoelectronic performance of mixed organic-inorganic halide perovskites has been at least partially attributed to their very high internal luminescence yield due partially to their so-called photon recycling ability [59–61]. This serves to provide an open circuit voltage closer to ideal values dictated by thermodynamics. Here, therefore, it is suggested that the limited loss of V_{oc} upon irradiation is partially related to radiative recombination at parasitic or unintentional interfaces induced by radiation exposure, but the subsequent recycling of photons in the absorber [60]. Similar effects were also recently observed in FAMACs solar cells assessed under LILT conditions [62]. The presence of non-radiative centers or the increase of radiative defects near the band edges are evident in the photoluminescence from the sample at 300 K before and after irradiation in Fig. 5(d). With irradiation, a low energy tail to the PL clearly signifies the presence of defects and/or impurity related emission which has been attributed to tin vacancies and interstitial iodide [58] that increase with exposure to the high energy protons. Additionally, the integrated intensity decreased considerably. The tolerance to such defects in device performance is attributed to the nature of this mixed Pb–Sn material, which incorporates defects prominently through the formation of Sn-vacancies - making the materials extrinsically p-type [37,40,63] - and under irradiation, primarily through I displacement due to the prevalence of this ion in the lattice. Although further studies are required, here it is proposed that while the irradiation of the devices results in additional defects, these are not prohibitive or more detrimental due to the background impurity concentration, which serves to passivate these additional defects. Additionally, the mobility of the ions at room temperature may still be under debate and can vary depending on composition [64], but are believed to have activation energies (100's meV) much less than that of gallium vacancies in GaAs (4 eV) [65]. This could result in the displaced iodide ions in the lattice, by energy transfer or collision events, effectively diffusing back into the lattice site thereby “self-healing.” Others have speculated at the implantation of the protons could effectively heal the organic cations at the surfaces and interfaces [19]. This is supported by the EQE shape before and after irradiation, which indicates the minority carrier diffusion length does not significantly change upon proton radiation. Such passivation would inevitably reduce the background doping and reduce the conductivity in the films, which has been observed in these systems previously [37].

In mixed Sn–Pb perovskites the formation of defects tends to occur at interfaces and surfaces [36,38] and as such have the potential to create non ideal interfaces and inhibit carrier extraction. Moreover, the background impurity concentration in the absorber can have strong implications on the position of the fermi-level and valence band maximum in the $(FASn)_{0.6}(MAPb)_{0.4}I_3$ blocking carrier extraction and increasing the series resistance [63]. These results indicate not only that perovskite systems are significantly radiation tolerant, but that the current architectures optimized for terrestrial applications require further consideration with respect to space conditions and indeed the specific mission, where temperature and/or irradiation conditions can significantly modify the band offsets, interfacial properties, and carrier transport in the solar cell structure.

While the radiation tolerance of the perovskite systems appears to significantly out-perform other PV technologies for space, more work must be done to investigate the tolerance to thermal cycling and temperature fluctuations under high vacuum. Indeed, the mixed Sn–Pb systems studied here demonstrate considerable degradation under thermal cycling, which while not presented here, represents a considerable limitation to their practical implementation in space power applications, currently giving thin film CIGS the advantage. However, these properties are not *a priori* a fundamental limitation to the potential of perovskites for lightweight space power applications, with recent advances in the stability of mixed cation and halide perovskites, along with stability improvements in Sn-based perovskites and encapsulation methods [66–68] suggesting the current limitations are not

insurmountable.

4. Conclusions

Here, the radiation tolerance of $(FASn)_{0.6}(MAPb)_{0.4}I_3$ solar cells typically used as the low energy junction of all perovskite 2 J junction tandems is assessed at levels consistent with several years of polar orbit. These perovskite systems appear to perform best at 260 K and are remarkably radiation tolerant to proton fluences *in excess of* 1×10^{11} protons/cm², with the absorber layer relatively unaffected by proton irradiation at energies and fluences that are prohibitive for traditional III-V or silicon PV systems. Moreover, in comparison to thin film CIGS - under similar conditions - the perovskites out-perform CIGS systems to levels in which irreversible damage results in these commercial thin film systems [31]. The significant radiation tolerance of perovskites is attributed to the details of defect formation in the material, which leads to interfacial or energy mismatches in the transport layers within the structure rather than mid gap defect centers that arise in more traditional systems.

CRedit authorship contribution statement

Brandon K. Durant: Conceptualization, Methodology, Formal analysis, Investigation, Data curation, Writing – original draft, Writing – review & editing, Visualization, Supervision. **Hadi Afshari:** Validation, Investigation. **Shashi Sourabh:** Validation, Investigation. **Vishal Yeddu:** Methodology, Validation, Investigation. **Matthew T. Bamidele:** Methodology, Validation, Investigation. **Satyabrata Singh:** Investigation, Software, Data curation. **Bibhudutta Rout:** Project administration, Conceptualization, Investigation, Software, Data curation, Supervision, Writing – original draft. **Giles E. Eperon:** Conceptualization, Resources. **Do Young Kim:** Project administration, Funding acquisition, Conceptualization, Supervision. **Ian R. Sellers:** Project administration, Funding acquisition, Conceptualization, Supervision, Writing – original draft, Writing – review & editing.

Declaration of competing interest

The authors declare that they have no known competing financial interests or personal relationships that could have appeared to influence the work reported in this paper.

Acknowledgements

This material is based upon work supported by the National Aeronautics and Space Administration under Agreement No. 80NSSC19M0140 issued through NASA Oklahoma EPSCoR.

Appendix A. Supplementary data

Supplementary data to this article can be found online at <https://doi.org/10.1016/j.solmat.2021.111232>.

References

- [1] National Renewable Energy Laboratory Research Cell Record Efficiency Chart. Best Research-Cell Efficiencies 2021.
- [2] S.A. Kulkarni, T. Baikie, P.P. Boix, N. Yantara, N. Mathews, S. Mhaisalkar, Band-gap tuning of lead halide perovskites using a sequential deposition process, *J. Mater. Chem.* 2 (2014) 9221–9225, <https://doi.org/10.1039/C4TA00435C>.
- [3] W. Shockley, H.J. Queisser, Detailed balance limit of efficiency of p-n junction solar cells, *J. Appl. Phys.* 32 (1961) 510–519, <https://doi.org/10.1063/1.1736034>.
- [4] T. Leijtens, K.A. Bush, R. Prasanna, M.D. McGehee, Opportunities and challenges for tandem solar cells using metal halide perovskite semiconductors, *Nature Energy* 3 (2018) 828–838, <https://doi.org/10.1038/s41560-018-0190-4>.
- [5] L.C. Hirst, N.J. Ekins-Daukes, Fundamental losses in solar cells, *Prog. Photovoltaics Res. Appl.* 19 (2011) 286–293, <https://doi.org/10.1002/pip.1024>.
- [6] J. Xu, C.C. Boyd, Z.J. Yu, A.F. Palmstrom, D.J. Witter, B.W. Larson, R.M. France, J. Werner, S.P. Harvey, E.J. Wolf, W. Weigand, S. Manzoor, M. van Hest, J.J. Berry,

- J.M. Luther, Z.C. Holman, M.D. McGehee, Triple-halide wide-band gap perovskites with suppressed phase segregation for efficient tandems, *Science* 367 (2020) 1097–1104, <https://doi.org/10.1126/science.aaz5074>.
- [7] K.A. Bush, A.F. Palmstrom, Z.J. Yu, M. Boccard, R. Cheacharoen, J.P. Mailoa, D. P. McMeekin, R.L.Z. Hoye, C.D. Bailie, T. Leijtens, I.M. Peters, M.C. Minichetti, N. Rolston, R. Prasanna, S. Sofia, D. Harwood, W. Ma, F. Moghadam, H.J. Snaith, T. Buonassisi, Z.C. Holman, S.F. Bent, M.D. McGehee, 23.6%-efficient monolithic perovskite/silicon tandem solar cells with improved stability, *Nature Energy* 2 (2017) 17009, <https://doi.org/10.1038/nenergy.2017.9>.
- [8] M. Langenhorst, B. Sautter, R. Schmager, J. Lehr, E. Ahlswede, M. Powalla, U. Lemmer, B.S. Richards, U.W. Paetzold, Energy yield of all thin-film perovskite/CIGS tandem solar modules, *Prog. Photovoltaics Res. Appl.* 27 (2019) 290–298, <https://doi.org/10.1002/pip.3091>.
- [9] A. Al-Ashouri, A. Magomedov, M. Roß, M. Joßt, M. Talaikis, G. Chistiakova, T. Bertram, J.A. Márquez, E. Köhnen, E. Kasparavičius, S. Levenco, L. Gil-Escrig, C.J. Hages, R. Schlattmann, B. Rech, T. Malinauskas, T. Unold, C.A. Kaufmann, L. Korte, G. Niaura, V. Getautis, S. Albrecht, Conformal monolayer contacts with lossless interfaces for perovskite single junction and monolithic tandem solar cells, *Energy Environ. Sci.* 12 (2019) 3356–3369, <https://doi.org/10.1039/C9EE02268F>.
- [10] Q. Han, Y.-T. Hsieh, L. Meng, J.-L. Wu, P. Sun, E.-P. Yao, S.-Y. Chang, S.-H. Bae, T. Kato, V. Bermudez, Y. Yang, High-performance perovskite/Cu(In,Ga)Se₂ monolithic tandem solar cells, *Science* 361 (2018) 904–908, <https://doi.org/10.1126/science.aat5055>.
- [11] D. Zhao, Y. Yu, C. Wang, W. Liao, N. Shrestha, C.R. Grice, A.J. Cimaroli, L. Guan, R. J. Ellingson, K. Zhu, X. Zhao, R.-G. Xiong, Y. Yan, Low-bandgap mixed tin-lead iodide perovskite absorbers with long carrier lifetimes for all-perovskite tandem solar cells, *Nature Energy* 2 (2017) 17018, <https://doi.org/10.1038/nenergy.2017.18>.
- [12] C. Li, Z. Song, C. Chen, C. Xiao, B. Subedi, S.P. Harvey, N. Shrestha, K.K. Subedi, L. Chen, D. Liu, Y. Li, Y.-W. Kim, C.-s. Jiang, M.J. Heben, D. Zhao, R.J. Ellingson, N. J. Podraza, M. Al-Jassim, Y. Yan, Low-bandgap mixed tin-lead iodide perovskites with reduced methylammonium for simultaneous enhancement of solar cell efficiency and stability, *Nature Energy* 5 (2020) 768–776, <https://doi.org/10.1038/s41560-020-00692-7>.
- [13] G.E. Eperon, T. Leijtens, K.A. Bush, R. Prasanna, T. Green, J.T.-W. Wang, D. P. McMeekin, G. Volonakis, R.L. Milot, R. May, A. Palmstrom, D.J. Slotcavage, R. A. Belisle, J.B. Patel, E.S. Parrott, R.J. Sutton, W. Ma, F. Moghadam, B. Conings, A. Babayigit, H.-G. Boyen, S. Bent, F. Giustino, L.M. Herz, M.B. Johnston, M. D. McGehee, H.J. Snaith, Perovskite-perovskite tandem photovoltaics with optimized band gaps, *Science* 354 (2016) 861–865, <https://doi.org/10.1126/science.aaf9717>.
- [14] A. Rajagopal, Z. Yang, S.B. Jo, I.L. Braly, P.-W. Liang, H.W. Hillhouse, A.K.-Y. Jen, Highly efficient perovskite-perovskite tandem solar cells reaching 80% of the theoretical limit in photovoltage, *Adv. Mater.* 29 (2017) 1702140, <https://doi.org/10.1002/adma.201702140>.
- [15] C.C. Boyd, R.C. Shallock, T. Moot, R. Kerner, L. Bertoluzzi, A. Onno, S. Kavadiya, C. Chosy, E.J. Wolf, J. Werner, J.A. Raiford, C. de Paula, A.F. Palmstrom, Z.J. Yu, J. J. Berry, S.F. Bent, Z.C. Holman, J.M. Luther, E.L. Ratcliff, N.R. Armstrong, M. D. McGehee, Overcoming redox reactions at perovskite-nickel oxide interfaces to boost voltages in perovskite solar cells, *Joule* 4 (2020) 1759–1775, <https://doi.org/10.1016/j.joule.2020.06.004>.
- [16] Z.M. Kassas, J. Khalife, New-age satellite-based navigation – STAN: simultaneous tracking and navigation with LEO satellite signals, *Inside GNSS Magazine* 14 (2019) 56–65.
- [17] A.S. Barthel, Larkin, Felix Lang, Gunnar Kusch, Jürgen Bundesmann, Andrea Denker, Rachel Oliver, Louise Hirst, Cathodoluminescence study of 68 MeV proton-irradiated ultra-thin GaAs solar cells, *IEEE PVSC* 46 (2020).
- [18] G.A. Landis, J. Fincannon, Study of power options for Jupiter and outer planet missions, in: 2015 IEEE 42nd Photovoltaic Specialist Conference (PVSC), 2015, pp. 1–5, <https://doi.org/10.1109/PVSC.2015.7356136>.
- [19] F. Lang, N.H. Nickel, J. Bundesmann, S. Seidel, A. Denker, S. Albrecht, V.V. Brus, J. Rappich, B. Rech, G. Landi, H.C. Neitzert, Radiation hardness and self-healing of perovskite solar cells, *Adv. Mater.* 28 (2016) 8726–8731, <https://doi.org/10.1002/adma.201603326>.
- [20] V.V. Brus, F. Lang, J. Bundesmann, S. Seidel, A. Denker, B. Rech, G. Landi, H. C. Neitzert, J. Rappich, N.H. Nickel, Defect dynamics in proton irradiated CH₃NH₃PbI₃ perovskite solar cells, *Advanced Electronic Materials* 3 (2017) 1600438, <https://doi.org/10.1002/aeml.201600438>.
- [21] F. Lang, M. Joßt, J. Bundesmann, A. Denker, S. Albrecht, G. Landi, H.-C. Neitzert, J. Rappich, N.H. Nickel, Efficient minority carrier detrapping mediating the radiation hardness of triple-cation perovskite solar cells under proton irradiation, *Energy Environ. Sci.* 12 (2019) 1634–1647, <https://doi.org/10.1039/C9EE00077A>.
- [22] F. Lang, M. Joßt, K. Frohna, E. Köhnen, A. Al-Ashouri, A.R. Bowman, T. Bertram, A. B. Morales-Vilches, D. Koushik, E.M. Tennyson, K. Galkowski, G. Landi, M. Creatore, B. Stannowski, C.A. Kaufmann, J. Bundesmann, J. Rappich, B. Rech, A. Denker, S. Albrecht, H.-C. Neitzert, N.H. Nickel, S.D. Stranks, Proton radiation hardness of perovskite tandem photovoltaics, *Joule* 4 (2020) 1054–1069, <https://doi.org/10.1016/j.joule.2020.03.006>.
- [23] Y. Miyazawa, M. Ikegami, H.-W. Chen, T. Ohshima, M. Imaizumi, K. Hirose, T. Miyasaka, Tolerance of perovskite solar cell to high-energy particle irradiations in space environment, *iScience* 2 (2018) 148–155, <https://doi.org/10.1016/j.isci.2018.03.020>.
- [24] S. Kanaya, G.M. Kim, M. Ikegami, T. Miyasaka, K. Suzuki, Y. Miyazawa, H. Toyota, K. Osonoe, T. Yamamoto, K. Hirose, Proton irradiation tolerance of high-efficiency perovskite absorbers for space applications, *J. Phys. Chem. Lett.* 10 (2019) 6990–6995, <https://doi.org/10.1021/acs.jpclett.9b02665>.
- [25] N. Nickel, F. Lang, V. Brus, J. Bundesmann, S. Seidel, A. Denker, S. Albrecht, G. Landi, H. Neitzert, Radiation Hardness and Self-Healing of Perovskite Solar Cells under Proton Irradiation (Conference Presentation), *SPIE*, 2018.
- [26] J. Huang, M.D. Kelzenberg, P. Espinet-González, C. Mann, D. Walker, A. Naqvi, N. Vaidya, E. Warmann, H.A. Atwater, Effects of electron and proton radiation on perovskite solar cells for space solar power application, in: 2017 IEEE 44th Photovoltaic Specialist Conference, PVSC, 2017, pp. 1248–1252, <https://doi.org/10.1109/PVSC.2017.8366410>.
- [27] A.K. Deb, V. Kumar, Ab initio design of CsSn(XxY 1–x)3 (X and Y = Cl, Br, and I) perovskites for photovoltaics, *AIP Adv.* 5 (2015), 077158, <https://doi.org/10.1063/1.4927503>.
- [28] K. Nishimura, M.A. Kamarudin, D. Hirotsani, K. Hamada, Q. Shen, S. Iikubo, T. Minemoto, K. Yoshino, S. Hayase, Lead-free tin-halide perovskite solar cells with 13% efficiency, *Nano. Energy* 74 (2020) 104858, <https://doi.org/10.1016/j.nanoen.2020.104858>.
- [29] B. Zhao, M. Abdi-Jalebi, M. Tabachnyk, H. Glass, V.S. Kamboj, W. Nie, A. J. Pearson, Y. Puttison, K.C. Gödel, H.E. Beere, D.A. Ritchie, A.D. Mohite, S. E. Dutton, R.H. Friend, A. Sadhanala, High open-circuit voltages in tin-rich low-bandgap perovskite-based planar heterojunction photovoltaics, *Adv. Mater.* 29 (2017) 1604744, <https://doi.org/10.1002/adma.201604744>.
- [30] C.C. Stoumpos, C.D. Malliakas, M.G. Kanatzidis, Semiconducting tin and lead iodide perovskites with organic cations: phase transitions, high mobilities, and near-infrared photoluminescent properties, *Inorg. Chem.* 52 (2013) 9019–9038, <https://doi.org/10.1021/ic401215x>.
- [31] H. Afshari, B.K. Durant, C.R. Brown, K. Hossain, D. Poptavskyy, B. Rout, I. R. Sellers, The role of metastability and concentration on the performance of CIGS solar cells under Low-Intensity-Low-Temperature conditions, *Sol. Energy Mater. Sol. Cells* 212 (2020) 110571, <https://doi.org/10.1016/j.solmat.2020.110571>.
- [32] C.R. Brown, V.R. Whiteside, D. Poptavskyy, K. Hossain, M.S. Dhoubhadel, I. R. Sellers, Flexible Cu(In,Ga)Se₂ solar cells for outer planetary missions: investigation under low-intensity low-temperature conditions, *IEEE Journal of Photovoltaics* 9 (2019) 552–558, <https://doi.org/10.1109/JPHOTOV.2018.2889179>.
- [33] W. Liao, D. Zhao, Y. Yu, N. Shrestha, K. Ghimire, C.R. Grice, C. Wang, Y. Xiao, A. J. Cimaroli, R.J. Ellingson, N.J. Podraza, K. Zhu, R.-G. Xiong, Y. Yan, Fabrication of efficient low-bandgap perovskite solar cells by combining formamidinium tin iodide with methylammonium lead iodide, *J. Am. Chem. Soc.* 138 (2016) 12360–12363, <https://doi.org/10.1021/jacs.6b08337>.
- [34] J.F. Ziegler, M.D. Ziegler, J.P. Biersack, Srim – the stopping and range of ions in matter, *Nucl. Instrum. Methods Phys. Res. Sect. B Beam Interact. Mater. Atoms* 268 (2010) 1818–1823, <https://doi.org/10.1016/j.nimb.2010.02.091>.
- [35] B. Rout, M.S. Dhoubhadel, P.R. Poudel, V.C. Kummari, B. Pandey, N.T. Deoli, W. J. Lakshantha, S.J. Mulware, J. Baxley, J.E. Manuel, J.L. Pacheco, S. Szilasi, D. L. Weathers, T. Reinert, G.A. Glass, J.L. Duggan, F.D. McDaniel, An overview of the facilities, activities, and developments at the university of North Texas ion beam modification and analysis laboratory (IBMAL), *AIP Conference Proceedings* 1544 (2013) 11–18, <https://doi.org/10.1063/1.4813454>.
- [36] L.E. Mundt, J. Tong, A.F. Palmstrom, S.P. Dunfield, K. Zhu, J.J. Berry, L. T. Schelhas, E.L. Ratcliff, Surface-activated corrosion in tin-lead halide perovskite solar cells, *ACS Energy Letters* (2020), <https://doi.org/10.1021/acsenylett.0c01445>.
- [37] M.T. Klug, R.L. Milot, J.B. Patel, T. Green, H.C. Sansom, M.D. Farrar, A. J. Ramadan, S. Martani, Z. Wang, B. Wenger, J.M. Ball, L. Langshaw, A. Petrozza, M.B. Johnston, L.M. Herz, H.J. Snaith, Metal composition influences optoelectronic quality in mixed-metal lead-tin triiodide perovskite solar absorbers, *Energy Environ. Sci.* 13 (2020) 1776–1787, <https://doi.org/10.1039/D0EE00132E>.
- [38] R. Prasanna, T. Leijtens, S.P. Dunfield, J.A. Raiford, E.J. Wolf, S.A. Swifter, J. Werner, G.E. Eperon, C. de Paula, A.F. Palmstrom, C.C. Boyd, M.F.A.M. van Hest, S.F. Bent, G. Teeter, J.J. Berry, M.D. McGehee, Design of low bandgap tin-lead halide perovskite solar cells to achieve thermal, atmospheric and operational stability, *Nature Energy* 4 (2019) 939–947, <https://doi.org/10.1038/s41560-019-0471-6>.
- [39] C. Yu, Z. Chen, J.J. Wang, W. Pfenninger, N. Vockic, J.T. Kenney, K. Shum, Temperature dependence of the band gap of perovskite semiconductor compound CsSnI₃, *J. Appl. Phys.* 110 (2011), 063526, <https://doi.org/10.1063/1.3638699>.
- [40] E.S. Parrott, T. Green, R.L. Milot, M.B. Johnston, H.J. Snaith, L.M. Herz, Interplay of structural and optoelectronic properties in formamidinium mixed tin-lead triiodide perovskites, *Adv. Funct. Mater.* 28 (2018) 1802803, <https://doi.org/10.1002/adfm.201802803>.
- [41] L.D. Whalley, J.M. Skelton, J.M. Frost, A. Walsh, Phonon anharmonicity, lifetimes, and thermal transport in CH₃NH₃PbI₃ from many-body perturbation theory, *Phys. Rev. B* 94 (2016) 220301, <https://doi.org/10.1103/PhysRevB.94.220301>.
- [42] R. Saive, S-shaped current-voltage characteristics in solar cells: a review, *IEEE Journal of Photovoltaics* 9 (2019) 1477–1484, <https://doi.org/10.1109/JPHOTOV.2019.2930409>.
- [43] E.C. Schueller, G. Laurita, D.H. Fabin, C.C. Stoumpos, M.G. Kanatzidis, R. Seshadri, Crystal structure evolution and notable thermal expansion in hybrid perovskites formamidinium tin iodide and formamidinium lead bromide, *Inorg. Chem.* 57 (2018) 695–701, <https://doi.org/10.1021/acs.inorgchem.7b02576>.
- [44] A. Francisco-López, B. Charles, O.J. Weber, M.I. Alonso, M. Garriga, M. Campoy-Quiles, M.T. Weller, A.R. Goñi, Equal footing of thermal expansion and electron-phonon interaction in the temperature dependence of lead halide perovskite band gaps, *J. Phys. Chem. Lett.* 10 (2019) 2971–2977, <https://doi.org/10.1021/acs.jpclett.9b00876>.

- [45] A.M. Nardes, M. Kemerink, R.A.J. Janssen, J.A.M. Bastiaansen, N.M.M. Kiggen, B. M.W. Langeveld, A.J.J.M. van Breemen, M.M. de Kok, Microscopic understanding of the anisotropic conductivity of PEDOT:PSS thin films, *Adv. Mater.* 19 (2007) 1196–1200, <https://doi.org/10.1002/adma.200602575>.
- [46] J. Zhou, D.H. Anjum, L. Chen, X. Xu, I.A. Ventura, L. Jiang, G. Lubineau, The temperature-dependent microstructure of PEDOT/PSS films: insights from morphological, mechanical and electrical analyses, *J. Mater. Chem. C* 2 (2014) 9903–9910, <https://doi.org/10.1039/C4TC01593B>.
- [47] T. Moot, J. Werner, G.E. Eperon, K. Zhu, J.J. Berry, M.D. McGehee, J.M. Luther, Choose your own adventure: fabrication of monolithic all-perovskite tandem photovoltaics, *Adv. Mater.* 32 (2020) 2003312, <https://doi.org/10.1002/adma.202003312>.
- [48] J. Tong, Z. Song, D.H. Kim, X. Chen, C. Chen, A.F. Palmstrom, P.F. Ndione, M. O. Reese, S.P. Dunfield, O.G. Reid, J. Liu, F. Zhang, S.P. Harvey, Z. Li, S. T. Christensen, G. Teeter, D. Zhao, M.M. Al-Jassim, M.F.A.M. van Hest, M.C. Beard, S.E. Shaheen, J.J. Berry, Y. Yan, K. Zhu, Carrier lifetimes of >1 μ s in Sn-Pb perovskites enable efficient all-perovskite tandem solar cells, *Science* 364 (2019) 475–479, <https://doi.org/10.1126/science.aav7911>.
- [49] R. Lin, K. Xiao, Z. Qin, Q. Han, C. Zhang, M. Wei, M.I. Saidaminov, Y. Gao, J. Xu, M. Xiao, A. Li, J. Zhu, E.H. Sargent, H. Tan, Monolithic all-perovskite tandem solar cells with 24.8% efficiency exploiting comproportionation to suppress Sn(II) oxidation in precursor ink, *Nature Energy* 4 (2019) 864–873, <https://doi.org/10.1038/s41560-019-0466-3>.
- [50] A.F. Palmstrom, G.E. Eperon, T. Leijtens, R. Prasanna, S.N. Habisreutinger, W. Nemeth, E.A. Gaulding, S.P. Dunfield, M. Reese, S. Nanayakkara, T. Moot, J. Werner, J. Liu, B. To, S.T. Christensen, M.D. McGehee, M.F.A.M. van Hest, J. M. Luther, J.J. Berry, D.T. Moore, Enabling flexible all-perovskite tandem solar cells, *Joule* 3 (2019) 2193–2204, <https://doi.org/10.1016/j.joule.2019.05.009>.
- [51] D. Zhao, C. Wang, Z. Song, Y. Yu, C. Chen, X. Zhao, K. Zhu, Y. Yan, Four-Terminal all-perovskite tandem solar cells achieving power conversion efficiencies exceeding 23%, *ACS Energy Letters* 3 (2018) 305–306, <https://doi.org/10.1021/acscenergylett.7b01287>.
- [52] D. Zhao, C. Chen, C. Wang, M.M. Junda, Z. Song, C.R. Grice, Y. Yu, C. Li, B. Subedi, N.J. Podraza, X. Zhao, G. Fang, R.-G. Xiong, K. Zhu, Y. Yan, Efficient two-terminal all-perovskite tandem solar cells enabled by high-quality low-bandgap absorber layers, *Nature Energy* 3 (2018) 1093–1100, <https://doi.org/10.1038/s41560-018-0278-x>.
- [53] B. Abdollahi Nejjand, I.M. Hossain, M. Jakoby, S. Moghadamzadeh, T. Abzieher, S. Gharibzadeh, J.A. Schwenzer, P. Nazari, F. Schackmar, D. Hauschild, L. Weinhardt, U. Lemmer, B.S. Richards, I.A. Howard, U.W. Paetzold, Vacuum-assisted growth of low-bandgap thin films (FA0.8MA0.2Sn0.5Pb0.5I3) for all-perovskite tandem solar cells, *Advanced Energy Materials* 10 (2020) 1902583, <https://doi.org/10.1002/aenm.201902583>.
- [54] D. Heynderickx, B. Quaghebeur, J. Wera, E.J. Daly, H.D.R. Evans, New radiation environment and effects models in the European space agency's space environment information system (SPENVIS), *Space Weather* (2004) 2, <https://doi.org/10.1029/2004SW000073>.
- [55] D.R. Ceratti, Y. Rakita, L. Cremonesi, R. Tenne, V. Kalchenko, M. Elbaum, D. Oron, M.A.C. Potenza, G. Hodes, D. Cahen, Self-healing inside APbBr3 halide perovskite crystals, *Adv. Mater.* 30 (2018) 1706273, <https://doi.org/10.1002/adma.201706273>.
- [56] D.-Y. Son, J.-W. Lee, Y.J. Choi, I.-H. Jang, S. Lee, P.J. Yoo, H. Shin, N. Ahn, M. Choi, D. Kim, N.-G. Park, Self-formed grain boundary healing layer for highly efficient CH3NH3PbI3 perovskite solar cells, *Nature Energy* 1 (2016) 16081, <https://doi.org/10.1038/nenergy.2016.81>.
- [57] A.J. Ferguson, R. Farshchi, P.K. Paul, P. Dippo, J. Bailey, D. Poplavskyy, A. Khanam, F. Tuomisto, A.R. Arehart, D. Kuciauskas, Defect-mediated metastability and carrier lifetimes in polycrystalline (Ag,Cu)(In,Ga)Se2 absorber materials, *J. Appl. Phys.* 127 (2020) 215702, <https://doi.org/10.1063/1.5134502>.
- [58] D. Meggiolaro, D. Ricciarelli, A.A. Alasmari, F.A.S. Alasmari, F. De Angelis, Tin versus lead redox chemistry modulates charge trapping and self-doping in tin/lead iodide perovskites, *J. Phys. Chem. Lett.* 11 (2020) 3546–3556, <https://doi.org/10.1021/acs.jpcclett.0c00725>.
- [59] L.M. Pazos-Outón, M. Szumilo, R. Lamboll, J.M. Richter, M. Crespo-Quesada, M. Abdi-Jalebi, H.J. Beeson, M. Vrucinic, M. Alsari, H.J. Snaith, B. Ehrler, R. H. Friend, F. Deschler, Photon recycling in lead iodide perovskite solar cells, *Science* 351 (2016) 1430–1433, <https://doi.org/10.1126/science.aaf1168>.
- [60] E. Yablonovitch, Lead halides join the top optoelectronic league, *Science* 351 (2016), <https://doi.org/10.1126/science.aaf4603>, 1401–1401.
- [61] Y. Fang, H. Wei, Q. Dong, J. Huang, Quantification of re-absorption and re-emission processes to determine photon recycling efficiency in perovskite single crystals, *Nat. Commun.* 8 (2017) 14417, <https://doi.org/10.1038/ncomms14417>.
- [62] C.R. Brown, G.E. Eperon, V.R. Whiteside, I.R. Sellers, Potential of high-stability perovskite solar cells for low-intensity–low-temperature (LILT) outer planetary space missions, *ACS Appl. Energy Mater.* 2 (2019) 814–821, <https://doi.org/10.1021/acsaem.8b01882>.
- [63] R.L. Milot, M.T. Klug, C.L. Davies, Z. Wang, H. Kraus, H.J. Snaith, M.B. Johnston, L. M. Herz, The effects of doping density and temperature on the optoelectronic properties of formamidinium tin triiodide thin films, *Adv. Mater.* 30 (2018) 1804506, <https://doi.org/10.1002/adma.201804506>.
- [64] Y. Yuan, J. Huang, Ion migration in organometal trihalide perovskite and its impact on photovoltaic efficiency and stability, *Acc. Chem. Res.* 49 (2016) 286–293, <https://doi.org/10.1021/acs.accounts.5b00420>.
- [65] M. Bockstedt, M. Scheffler, *Theory of Self-Diffusion in GaAs*, 1996 arXiv preprint [cond-mat/9612026](https://arxiv.org/abs/cond-mat/9612026).
- [66] L. Shi, M.P. Bucknall, T.L. Young, M. Zhang, L. Hu, J. Bing, D.S. Lee, J. Kim, T. Wu, N. Takamura, D.R. McKenzie, S. Huang, M.A. Green, A.W.Y. Ho-Baillie, Gas chromatography–mass spectrometry analyses of encapsulated stable perovskite solar cells, *Science* 368 (2020), <https://doi.org/10.1126/science.aba2412> eaba2412.
- [67] R. Cheacharoen, N. Rolston, D. Harwood, K.A. Bush, R.H. Dauskardt, M. D. McGehee, Design and understanding of encapsulated perovskite solar cells to withstand temperature cycling, *Energy Environ. Sci.* 11 (2018) 144–150, <https://doi.org/10.1039/C7EE02564E>.
- [68] A. Uddin, M.B. Upama, H. Yi, L. Duan, Encapsulation of organic and perovskite solar cells: a review, *Coatings* 9 (2019) 65.